Manuscript version: Author's Accepted Manuscript

The version presented in WRAP is the author's accepted manuscript and may differ from the published version or Version of Record.

Persistent WRAP URL:

http://wrap.warwick.ac.uk/166853

How to cite:

Please refer to published version for the most recent bibliographic citation information. If a published version is known of, the repository item page linked to above, will contain details on accessing it.

Copyright and reuse:

The Warwick Research Archive Portal (WRAP) makes this work by researchers of the University of Warwick available open access under the following conditions.

Copyright © and all moral rights to the version of the paper presented here belong to the individual author(s) and/or other copyright owners. To the extent reasonable and practicable the material made available in WRAP has been checked for eligibility before being made available.

Copies of full items can be used for personal research or study, educational, or not-for-profit purposes without prior permission or charge. Provided that the authors, title and full bibliographic details are credited, a hyperlink and/or URL is given for the original metadata page and the content is not changed in any way.

Publisher's statement:

Please refer to the repository item page, publisher's statement section, for further information.

For more information, please contact the WRAP Team at: wrap@warwick.ac.uk.

Room Temperature Electrochemical Fluoride (De)Insertion into the Defect Pyrochlore CsMnFeF$_6$

Jessica L. Andrews,[†] Eric T. McClure,[†] Kenneth K. Jew,[‡] Molleigh B. Preefer,[¶] Ahamed Irshad,[†] Matthew J. Lertola,[§] Daniel D. Robertson,[∥] Charlene Z. Salamat,[∥] Michael J. Brady,[†] Louis F. J. Piper,[⊥,#] Sarah H. Tolbert,[∥,@,△] Johanna Nelson Weker,[¶] Brad F. Chmelka,[§] Bruce S. Dunn,[@,△] Sri R. Narayan,[†] William C. West,[∇] and Brent C. Melot[*,†,‡]

[†]*Department of Chemistry, University of Southern California, Los Angeles, California 90089, USA*
[‡]*Department of Chemical Engineering and Materials Science, University of Southern California, Los Angeles, California 90089, USA*
[¶]*Stanford Synchrotron Radiation Lightsource, SLAC National Accelerator Laboratory, Menlo Park, California 94025, USA*
[§]*Department of Chemical Engineering, University of California, Santa Barbara, Santa Barbara, California 93106, USA*
[∥]*Department of Chemistry and Biochemistry, UCLA, Los Angeles, California 90095, USA*
[⊥]*Warwick Manufacturing Group, University of Warwick, Coventry, CV4 7AL, United Kingdom*
[#]*Department of Physics, Applied Physics and Astronomy, Binghamton University, Binghamton, New York 13902, USA*
[@]*Department of Materials Science and Engineering, UCLA, Los Angeles, California 90095, USA*
[△]*The California NanoSystems Institute, UCLA, Los Angeles, California 90095, USA*
[∇]*Jet Propulsion Laboratory, California Institute of Technology, Pasadena, California 91109, USA*

Abstract

We report on the reversible, electrochemical (de)fluorination of the defect fluoride pyrochlore CsMnFeF$_6$ at room temperature using a liquid electrolyte. CsMnFeF$_6$ was synthesized via three different synthetic methods (hydrothermal, ceramic, and mechanochemical), each of which yield products of varying particle size and phase purity. Using galvanostatic cycling, we found that after three oxidative/reductive cycles, approximately one fluoride ion can be reversibly inserted and removed from mechanochemically synthesized CsMnFeF$_6$ for multiple cycles. *Ex-situ* X-ray absorption spectroscopy confirmed that both the Mn^{2+} and Fe^{3+} in this composition are redox active during cycling. Electrochemical impedance spectroscopy and *ex-situ* synchrotron powder diffraction were utilized to investigate the delayed onset of significant fluoride (de)insertion. We observed decreased impedance after one full cycle and subtle expansion and contraction of the CsMnFeF$_6$ cubic lattice on oxidation (insertion) and reduction (removal), respectively, over the first two cycles. Our results suggest the formation of fluoride vacancies in early cycles generates mixed valence Fe that enhances the ionic and electronic conductivity, improving the reversibility in later cycles.

While research on cation intercalation has thrived and resulted in real world applications, like high energy density Li-ion batteries, little work has been done to understand the mechanism of anionic intercalation and its effects on a host's structure.[1,2] Given the numerous, impactful discoveries from research on cation intercalation, the potential for anionic intercalation is extremely promising. The possibility of anions serving as charge carriers for electrochemical energy storage provides an alternative frontier to explore a variety of new rechargeable battery materials. However, due to their significantly larger radii and negative charge, the diffusion of anions through densely packed solids requires significantly different conditions than that of mobile cations.[3] Developing an understanding of the structural changes induced by cation intercalation and diffusion in the solid state proved crucial to augmenting the performance of Li-ion batteries. Therefore, a pivotal starting point in the exploration of anionic intercalation is identifying the key structural features that enable and promote anionic diffusion in the solid state.

Thus far, the electrochemistry of smaller anions, such as fluoride, has been mostly limited to conversion-based systems, in which the electrode materials react during oxidation/reduction to form entirely new products, typically with drastically different structures and chemistries.[4–7] Fichtner and co-workers employed these conversion reactions to produce a rechargeable fluoride-

ion (F-ion) battery, utilizing a solid electrolyte in tandem with a CuF_2 cathode cycled against a La metal film anode.[8] When electrochemically cycled, this results in the reduction of the cathode to produce Cu metal and conversion of the anode to yield LaF_3. Although these are reversible reactions, F-ion cycling of conversion-based electrodes typically incurs large volume changes, resulting in poor cycling stability due to limited reversibility over multiple cycles.

More recently, systems that leverage fluoride intercalation, in which the host material may experience crystal structure changes but should broadly maintain its original topology and connectivity, have been reported. For example, Clemens and co-workers successfully showed intercalation of fluoride into $LaSrMnO_4$ and La_2CoO_4 using all-solid-state cell geometries.[9,10] However, the Ba-doped LaF_3 solid electrolyte utilized in these all-solid-state cells suffers from poor room temperature fluoride conductivity, thereby requiring operating temperatures of 150 °C or higher.[11–13] While there are also recent reports of systems that incorporate the solid electrolytes $PbSnF_4$ and $BaSnF_4$ to cycle fluoride reversibly at room temperature, they are based on conversion electrodes that suffer from significant capacity fade in the first few cycles.[14,15]

Thus, poor reversibility and high operating temperature requirements have limited any practical use of the reported F-ion systems. This emphasizes the need to develop intercalation-based electrodes that can reversibly (de)insert fluorides paired with electrolytes that exhibit significant fluoride mobility at ambient temperatures. Christe reported one of the first advances toward developing a room-temperature electrolyte with the stabilization of fluoride using quaternary ammonium salts in tetrahydrofuran (THF).[16] Davis *et al.* recently reported that solutions of the salt *N,N,N*-trimethyl-*N*-neopentylammonium fluoride (Np_1F) dissolved in fluoroether solvents enabled stable cycling of conversion cathodes composed of $CuF_2@LaF_3$ core–shell nanoparticles.[17] These works provided some of the first substantial evidence that small anions, like fluoride, can be leveraged electrochemically much like lithium cations can be, presenting an avenue to overcome the barriers that have thus far limited the study of anionic (de)intercalation.

Building off of these advances, our group recently reported on the electrochemical fluorination of an oxide host, ReO_3, from a liquid fluoride electrolyte, tetra-*n*-butylammonium fluoride (TBAF) dissolved in THF, at room temperature.[18] Although clear evidence for fluoride incorporation was obtained through a combination of electrochemical cycling, ^{19}F NMR techniques, and *operando* X-ray diffraction studies, reversible cycling of fluoride at room temperature was not achievable due to the instability of fluorinated ReO_3.[18]

Following this work, we began to explore the defect pyrochlore $CsMnFeF_6$ (Fig. 1).[19] Oxide pyrochlores are known to display high ionic conductivities[21,22] and the crystal structure contains multiple different anionic

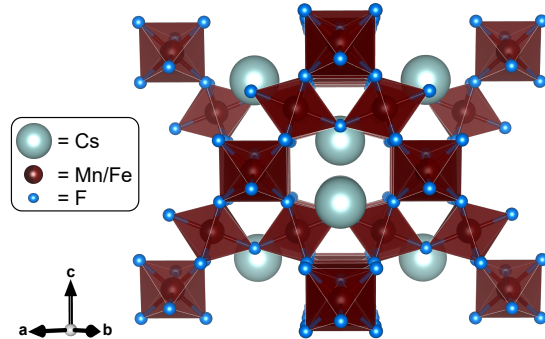Figure 1: Crystal structure of the defect fluoride pyrochlore, $CsMnFeF_6$, viewed down the [110] direction. Crystal structure depicted using VESTA.[20]

interstitials, including an ordered anionic vacancy,[23] which is promising for electrochemical fluoride intercalation. Ideal pyrochlores have the general formula $A_2B_2X_6Y$, where the A and B sites are filled by metal cations and the X and Y sites are filled by anions, like oxygen or fluorine. The structure is best viewed as two interpenetrating, three-dimensional frameworks of B_2X_6 and A_2Y.[23] The B_2X_6 substructure is comprised of corner-sharing BX_6 octahedra, forming a three-dimensional network of six-membered rings and, as a result, large hexagonal cavities. The A_2Y substructure resembles anticristobalite Cu_2O, with four-coordinate Y anions and two-coordinate A cations, and penetrates the B_2X_6 framework so that the A cations occupy the centers of the hexagonal cavities. As a result, there are three distinct anionic sites in the pyrochlore crystal structure: X, Y, and an ordered anionic vacancy. Ionic diffusion in pyrochlores is typically ascribed to vacancy hopping through a continuous path of second-nearest-neighbor X sites.[21,24] Since all of these sites must be occupied to maintain charge neutrality, diffusion through the network requires the presence of Frenkel defects, wherein an X site is vacant and an ordered vacancy site is filled by the missing X anion.[21,24] These pairs can be realized by introducing disorder at the B-site, which produces disorder between the X site and the vacant site.[21,24]

Appreciable ionic conductivity in pyrochlores therefore relies heavily on disorder within the B_2X_6 substructure, which is typically achieved via isovalent or aliovalent substitution.[21,22] In addition, various defect pyrochlores form readily because the A_2Y substructure can be absent or partially occupied.[25] Therefore, we hypothesized that the mixed B-site, defect pyrochlore $CsMn^{2+}Fe^{3+}F_6$ ($ABB'X_6$, Fig. 1) would make an ideal fluoride intercalation host as it possesses an ordered anionic vacancy and should display relatively high room temperature fluoride conductivity due to disorder in the $MnFeF_6$ substructure.

$CsMnFeF_6$ crystallizes in the cubic space group $Fd\bar{3}m$ (#227), as shown in Figure 1.[19] $CsMnFeF_6$ was synthesized via three different methods: "hydrothermal",
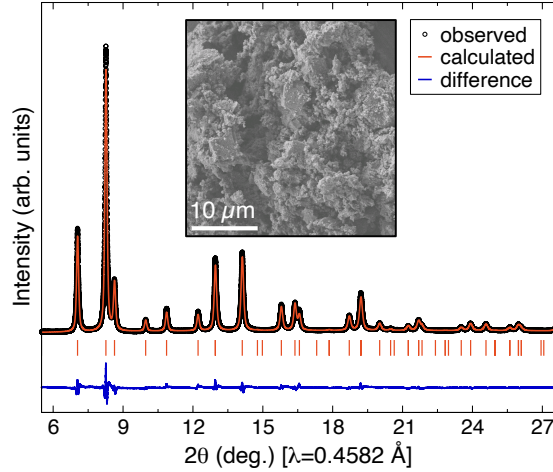
Figure 2: Rietveld refinement of synchrotron PXRD data for mechanochemical $CsMnFeF_6$. Inset: SEM image of mechanochemical $CsMnFeF_6$.

"ceramic", and "mechanochemical", described in detail in the Supporting Information. Rietveld refinements of the structure against synchrotron powder X-ray diffraction (PXRD) data were performed to evaluate the phase purity obtained from each synthetic method, with the resulting structural parameters given in SI Tables #S2–4. While the mechanochemical reaction was found to yield a high degree of purity (Fig. 2), the hydrothermal and ceramic materials contained mixtures of $CsMnFeF_6$, $CsMnF_3$, MnF_2, and $CsMnFe_2F_9$ (Fig. S1a and S2a). It is important to note that none of these impurities were seen using in-house diffraction, and it was only the high intensity of the synchrotron source that revealed the secondary phases.

Scanning electron microscopy (SEM) images show that of the three methods, the hydrothermal method produces the largest, most uniformly shaped particles, the ceramic technique yields the smallest, and the mechanochemical approach yields the least uniformly shaped and sized particles. The hydrothermal $CsMnFeF_6$ particles were roughly ~ 10 μm in diameter and exhibited an octahedral habit with broad (111) facets, similar to previous reports (see the inset of Fig. S1a).[26] The ceramic $CsMnFeF_6$ method yields the smallest particles, between 1 and 5 μm in diameter, with no clearly defined shape (Fig. S2a inset). In contrast, the particles from the mechanochemical method are irregularly shaped and exhibit the widest range of sizes, anywhere from <1 μm to >10 μm (Fig. 2a inset). Despite the variation in particle size and morphology observed in the SEM, X-ray photoelectron spectroscopy (XPS) results indicate all three synthetic methods produce particles with surfaces terminated by mostly Cs and F (Fig. S4–S6).

Materials prepared with each method were electrochemically cycled using Bi/BiF_3 composite counter electrodes, which provide a stable counter electrode over long-term cycling compared to MF_x electrodes.[4,5,7,27] Glass fiber separators (Whatman GF/D) were soaked in a commercial solution of 1.0 M TBAF in THF, which served as the electrolyte. TBAF was chosen based on prior work that showed a high fluoride conductivity at room temperature over a relatively wide electrochemical window.[18] Loose powder working electrodes, prepared by ball milling conductive carbon and $CsMnFeF_6$, were utilized.

As seen in Figure 3a, the first oxidation of the mechanochemical sample exhibits a smoothly sloped voltage curve that gradually flattens towards the upper voltage limit of 1.4 V vs. Bi/BiF_3 $[E_c^o(Bi^{3+}/Bi) = 3.4$ V vs. $Li^+/Li]$.[17] This first oxidation results in a specific capacity of 33 mAh/g, which exceeds 40% of the theoretical capacity (74.9 mAh/g), as calculated for the (de)insertion of one equivalent of fluoride per formula unit. The shape of the first reduction begins to exhibit four distinct regions of subtle differences in the voltage slope. In the first, there is a steep decrease from 1.4 to 1.0 V. From 1.0 to 0.75 V, the curve flattens slightly to form a short plateau before steepening from 0.75 to 0.4 V. The final region shows the most significant flattening of the voltage profile with a plateau from 0.4 to 0.0 V, for an overall capacity of 41 mAh/g. The second oxidation yields a profile that more closely resembles the reversal of the first reduction curve, rather than the limited capacity of the first oxidation.

By the third cycle, the voltage profile is more well-defined with the capacity exceeding 80% of the theoretical capacity on both oxidation and reduction, with only ~ 300 mV of polarization. The voltage profiles for
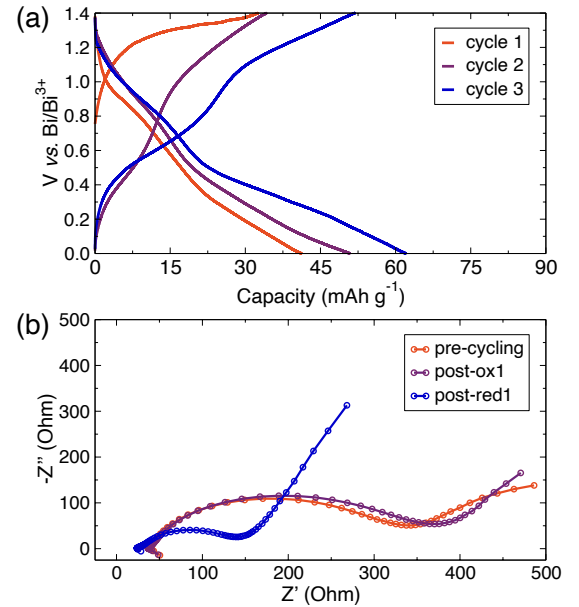

Figure 3: (a) Cycles 1–3 from galvanostatic cycling of a F-ion cell, with a working electrode of mechanochemically synthesized $CsMnFeF_6$ and a Bi/BiF_3 composite counter electrode, cycled at room temperature at a rate of C/20 between 0.0 and 1.4 V. (b) PEIS performed before cycling, after the first oxidative cycle (ox1), and after the first reductive cycle (red1).
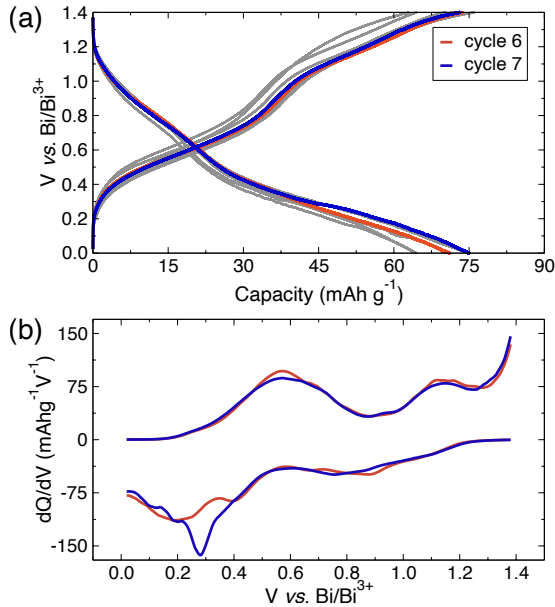
Figure 4: (a) Cycles 4–9 from galvanostatic cycling of a F-ion cell, with a working electrode of mechanochemically synthesized $CsMnFeF_6$ and a Bi/BiF_3 composite counter electrode, cycled at room temperature at a rate of C/20 between 0.0 and 1.4 V. Cycles six and seven are shown in orange and blue, respectively. (b) Differential capacity plot derived from the sixth and seventh cycles.

all subsequent cycles exhibit a similar profile (Fig. 4a), with sloped plateaus during oxidation (reduction) at approximately 0.6 V (0.4 V) and 1.15 V (0.85 V), as seen in the differential capacity curve in Fig. 4b. The reversible capacity reaches 70 mAh/g, which is very near the maximum theoretical capacity for one fluoride ion, and is maintained through the 9th cycle after which a gradual fade is seen.

The ceramic material cycled similarly to the mechanochemical material, although it showed less reversibility and a smaller Coulombic efficiency (Fig. S8). The entire first cycle exhibits a low capacity relative to the theoretical limit, and the faradaic features during the first reduction are very subtle. In contrast with the mechanochemical material's voltage profile, the ceramic material does not exhibit well-resolved faradaic features until the fourth reduction/fifth oxidation. This is unsurprising, as the ceramic sample contained several impurities that are unlikely to be redox active, so the poor performance may be attributable to a delayed onset of clear electrochemistry from fluoride (de)insertion into the $CsMnFeF_6$ phase.

From the fifth cycle onward, the galvanostatic cycling exhibits the clearly defined four-region voltage profile with sloped plateaus during oxidation (reduction) at approximately 0.7 V (0.3 V) and 1.3 V (0.9 V) (Fig. S8). The capacity also gradually increases, reaching a maximum of 58 mAh/g on the fifth reduction and 61 mAh/g on the sixth oxidation, corresponding to reversible fluoride (de)insertion but only achieving ~80% of the theoretical capacity. This average capacity is maintained

through the 8th cycle, but begins to fade after the 9th cycle. The ceramic material also exhibits a slightly larger voltage polarization (~400 mV) compared to that of the mechanochemical material (~300 mV). Therefore, the ceramic samples still cycle relatively well, but the maximum capacity is lower and fades more quickly than that of the mechanochemical samples.

In contrast, the hydrothermal samples do not cycle nearly as well as the others (Fig. S9). Despite exhibiting a similar voltage profile, they show the largest polarization and the least defined faradaic features. Similar to the mechanochemical and ceramic materials, the first cycle exhibits a very low capacity compared to the theoretical value. Akin to the ceramic material, the hydrothermal material does not exhibit well-resolved faradaic features until the fourth/fifth cycle. This is unsurprising because the hydrothermal material also contained redox inactive impurity phases (i.e., MnF_2), leading to a slower onset of clear electrochemistry from fluoride (de)insertion into $CsMnFeF_6$. After the fifth cycle, a sloping plateau is observed during oxidation (reduction) at approximately 0.8 V (0.3 V). However, the second, small plateau seen at higher voltages in the cycling of the other two materials is not observable in the hydrothermal cycling (Fig. S9). To explore whether the polarization of the cells was shifting this high voltage feature out of the cycling window, the upper limit was expanded to 1.45 V vs. BiF_3 (Fig. S9). While better reversibility was achieved, the higher voltage feature still could not be resolved and opening the window further lead to irreversible reactions that may correspond to fluorination of the carbon additive or attack of the electrolyte.[18,28,29]

The local bonding environments of the Fe atoms within $CsMnFeF_6$ were analyzed directly using zero-field ^{57}Fe Mössbauer spectroscopy, which is sensitive to the types and symmetry of coordinating ligands to Fe atoms based on the absorption of gamma rays by Fe nuclei in solid materials. Mössbauer spectra were acquired at room temperature for the three $CsMnFeF_6$ materials, a representative example of which is shown in Figure 5 for the mechanochemical material; the spectra for the other materials are shown in Figures S1b and S2b. Each of the Mössbauer spectra exhibits a dominant quadrupole doublet with an isomer shift, δ, of 0.3 mm/s, which is comparable to previously reported values for high-spin, octahedral Fe(III) sites in similar materials.[30,31] Identical quadrupole splittings, $|\Delta E_Q|$, of 0.3 mm/s are also observed for this dominant signal in all three spectra. The quadrupole splitting value, which tends to increase with the distortion of the electronic environment around high-spin Fe(III) ions, is lower than reported previously for similar pyrochlore materials,[30,32] reflecting more symmetric Fe(III) environments in the materials investigated here.

The spectra for the ceramic and mechanochemical $CsMnFeF_6$ samples exhibited a second, less intense quadrupole doublet with an isomer shift of 0.7 mm/s and a quadrupole splitting of 1.3 mm/s. This larger iso-
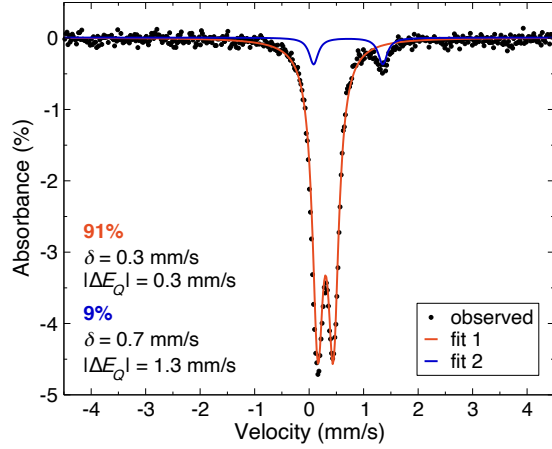
Figure 5: Mössbauer spectrum of mechanochemical $CsMnFeF_6$, collected at 298 K over approximately one day.

mer shift is indicative of an Fe(II) species,[31] which suggests that the ceramic and mechanochemical synthetic methods produce a small amount (∼9%) of mixed-valent Fe-sites, whereas the hydrothermal method does not. Overall, the consistent isomer shift and quadrupole splitting values for the dominant signal among the spectra for all three samples indicate that similar local Fe environments result from the different synthetic methods. The presence of a single doublet in the spectrum of the hydrothermally prepared $CsMnFeF_6$ suggests that fluoride is the predominant and probably only type of coordinating ligand near the Fe-sites in these materials.[33] If any F^- ligands were replaced with OH^- in the hydrothermal synthesis, then a second doublet with a larger quadrupole splitting would be present in the room-temperature Mössbauer spectrum, corresponding to differently coordinated Fe-sites.[33] Therefore, the Mössbauer spectroscopy results indicate that there is likely no OH^- impurity in the hydrothermal product, and that all three materials contain a majority of octahedral Fe(III).

Potentiostatic electrochemical impedance spectroscopy (PEIS) and galvanostatic cycling were performed on identical cells to investigate if the observed voltage profile changes in the initial cycles were reflected as changes in the total impedance of the cell (Fig. 3b, S8a, S9a insets). PEIS was conducted with a voltage amplitude of 10 mV, measured between frequencies of 1 MHz and 100 mHz, on each cell at three different points: (1) before any galvanostatic cycling, (2) after one oxidation, and (3) after one full cycle. Of the three samples, the hydrothermal material exhibits the highest initial impedance, whereas the ceramic and mechanochemical materials are very similar to one another. This is in agreement with trends in the Mössbauer spectroscopy, where samples prepared using the ceramic and mechanochemical methods exhibit significant amounts of Fe^{2+}, whereas the hydrothermal samples exclusively contain Fe^{3+}. This mixed

valency likely boosts the electronic conductivity of the mechanochemical and ceramic materials compared to the hydrothermal material. This is supported by the fact that all three materials show a minor increase in the impedance after one oxidation, which would remove the Fe^{2+} from the sample, thereby decreasing the electrical conductivity.Indeed, following the first reduction, more Fe^{3+} is converted to Fe^{2+}, and this mixed valency likely enhances the total conductivity regardless of the synthetic method employed.

Ex-situ synchrotron PXRD was performed to identify and study the structural impacts of fluoride (de)insertion into $CsMnFeF_6$. Electrodes from the mechanochemical method were stopped at four points during cycling: after the first oxidation (ox 1), after 1 full cycle (red 1), after 1 cycle and 1 oxidation (ox 2), and after 2 full cycles (red 2). Synchrotron powder XRD was collected at beamline 11-BM at the APS. The results of Rietveld refinements (given in Tables #S5–7) show a subtle lattice expansion on oxidation (insertion) and contraction on reduction (removal) in the first two cycles (Fig. 6, S7). Specifically, the cubic lattice parameter remains nearly constant on ox 1, contracts 0.12% on red 1, expands 0.08% on ox 2, and contracts 0.09% on red 2. This corresponds to a unit cell volume contraction of 0.34% on red 1, expansion of 0.25% on ox 2, and a contraction of 0.28% on red 2. Yet, no new reflections corresponding to any of the binary fluorides were observed in cycles 1–2, confirming that the changes in the voltage profile observed in the early cycles are not due to a conversion reaction The peaks around ∼8.05° 2θ can be attributed to Bi and BiF_3, which suggests some crossover due to dissolution at the counter electrode during cycling (Fig. S7).
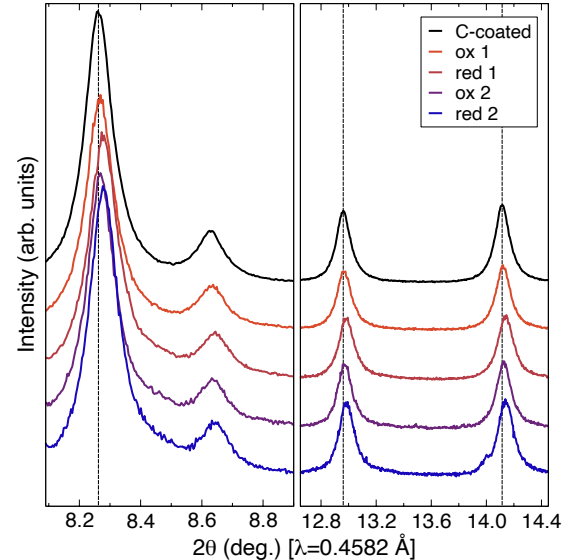
Ex-situ Mn K-edge and Fe K-edge X-ray absorp-

Figure 6: Zoomed in regions of *ex-situ* synchrotron PXRD results showing subtle shifts of the $CsMnFeF_6$ reflections corresponding to expansion on oxidation and contraction on reduction.

tion spectroscopy (XAS) experiments were performed at beamline 4-1 at SSRL to identify the redox couple(s) responsible for the observed electrochemical activity. In addition to measuring pristine and carbon-coated mechanochemical $CsMnFeF_6$, electrodes were harvested at two points during cycling: after 2 cycles and 1 oxidation (ox 3) and after 3 full cycles (red 3). The reported edge energies were defined using the zero-crossings of the second derivatives (Fig. S10, S11).

The Mn K-edge of pristine $CsMnFeF_6$ (6547.1 eV) is at a similar energy as that of the MnF_2 standard (6547.8 eV), suggesting the composition is predominantly in the Mn^{2+} state before cycling, as expected (Fig. 7a, S10). In the sample collected after oxidation, the Mn K-edge shifts to a higher energy (6551.8 eV), towards the MnF_3 standard's Mn K-edge (6554.1 eV), indicating that Mn^{2+} is being oxidized (Fig. 7a, S10). After reduction, the Mn K-edge shifts back to a lower energy (6547.8 eV), re-aligning with the Mn K-edge of the pristine material and confirming that the oxidation is reversible. However, the shape of the X-ray absorption near edge structure (XANES) is clearly very different for the pristine material compared to the two *ex-situ* samples, indicative of changes in the Mn coordination environment upon the (de)insertion of fluoride. A more comprehensive characterization of these structural changes will be reported in a forthcoming study of the local structure.

The Fe K-edge of pristine $CsMnFeF_6$ (7129.4 eV) is at a similar energy as that of the FeF_3 standard (7129.3 eV), suggesting the composition is predominantly in the Fe^{3+} state before cycling, as expected (Fig. 7b, S11). In the post-reduction sample (red 3), the Fe K-edge shifts to a lower energy (7124.7 eV), towards the Fe K-edge of the FeF_2 standard (7122.8 eV), indicating that the Fe^{3+} is being reduced (Fig. 7b, S11). After oxidation, the Fe K-edge shifts back to a higher energy (7129.5 eV), re-aligning with the Fe K-edge of the pristine material and confirming that the reduction is reversible. The shape of the XANES is relatively consistent between the pristine and cycled materials, suggesting the Fe coordination environment does not change significantly with the (de)insertion of fluoride. Therefore, the shifts in the Mn and Fe K-edges confirm that upon fluoride (de)insertion into $CsMnFeF_6$, both Mn^{2+} and Fe^{3+} are redox active.

The incomplete shift of the Mn and Fe K-edges observed for the *ex-situ* samples is consistent with the reversible capacity achieved. While the maximum capacity observed in the galvanostatic cycling was $\sim$75 mAh/g, the *ex-situ* XAS samples were collected during/after cycle 3, which typically only reaches 80% of the theoretical capacity. The observed redox activity of both Mn^{2+} and Fe^{3+} during cycling suggests that, theoretically, the capacity could be doubled to 149.9 mAh/g (two fluoride ions per formula unit). In other words, if Fe^{3+} could be fully reduced to Fe^{2+} on reduction and if Mn^{2+} were fully oxidized to Mn^{3+} on oxidation, multi-electron redox could be realized. Toward this ex-
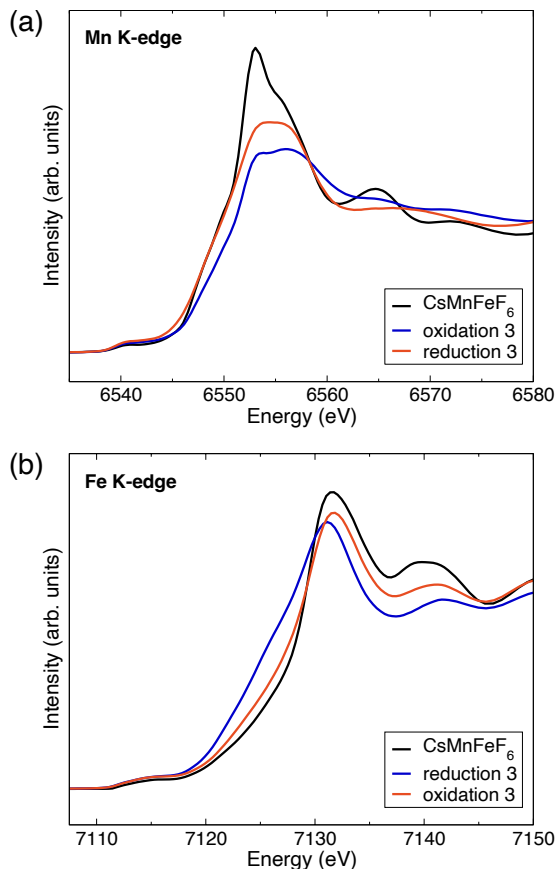

Figure 7: *Ex-situ* X-ray absorption spectroscopy results showing (a) the shifting Mn K-edge and (b) shifting Fe K-edge upon fluoride (de)insertion.

citing prospect, we are actively continuing to optimize our room-temperature F-ion cell geometry.

In summary, we present the first report of reversible (de)fluorination in the defect pyrochlore $CsMnFeF_6$ using a liquid electrolyte at room temperature. Using a combination of galvanostatic cycling and electrochemical impedance spectroscopy, we propose that an increase in fluoride vacancies and mixed valency at the Fe-sites occurs in the early cycles. *Ex-situ* XRD shows that $CsMnFeF_6$ undergoes a small but clearly reversible expansion on oxidation (fluoride insertion) and contraction following reduction (fluoride removal). In parallel, *ex-situ* XAS indicates that both the $Fe^{3+/2+}$ and $Mn^{3+/2+}$ redox couples are active during the cycling of $CsMnFeF_6$. This work suggests the potential for a paradigm shift from traditional Li-ion battery technologies.

Acknowledgements

References

(1) Whittingham, M. S. Lithium Batteries and Cathode Materials. *Chemical Reviews* **2004**, *104*, 4271–4302.

(2) Manthiram, A. A reflection on lithium-ion battery cathode chemistry. *Nature Communications* **2020**, *11*, 1550.

(3) West, W. C.; Whitacre, J. F.; Leifer, N.; Greenbaum, S.; Smart, M.; Bugga, R.; Blanco, M.; Narayanan, S. R. Reversible Intercalation of Fluoride-Anion Receptor Complexes in Graphite. *Journal of The Electrochemical Society* **2007**, *154*, A929.

(4) Gschwind, F.; Rodriguez-Garcia, G.; Sandbeck, D.; Gross, A.; Weil, M.; Fichtner, M.; Hörmann, N. Fluoride ion batteries: Theoretical performance, safety, toxicity, and a combinatorial screening of new electrodes. *Journal of Fluorine Chemistry* **2016**, *182*, 76–90.

(5) Grenier, A.; Porras-Gutierrez, A.-G.; Groult, H.; Beyer, K. A.; Borkiewicz, O. J.; Chapman, K. W.; Dambournet, D. Electrochemical reactions in fluoride-ion batteries: mechanistic insights from pair distribution function analysis. *J. Mater. Chem. A* **2017**, *5*, 15700–15705.

(6) Anji Reddy, M.; Fichtner, M. Batteries based on fluoride shuttle. *J. Mater. Chem.* **2011**, *21*, 17059–17062.

(7) Rongeat, C.; Anji Reddy, M.; Diemant, T.; Behm, R. J.; Fichtner, M. Development of new anode composite materials for fluoride ion batteries. *J. Mater. Chem. A* **2014**, *2*, 20861–20872.

(8) Thieu, D. T.; Fawey, M. H.; Bhatia, H.; Diemant, T.; Chakravadhanula, V. S. K.; Behm, R. J.; Kübel, C.; Fichtner, M. CuF_2 as Reversible Cathode for Fluoride Ion Batteries. *Advanced Functional Materials* **2017**, *27*, 1701051.

(9) Nowroozi, M. A.; Wissel, K.; Rohrer, J.; Munnangi, A. R.; Clemens, O. $LaSrMnO_4$: Reversible Electrochemical Intercalation of Fluoride Ions in the Context of Fluoride Ion Batteries. *Chemistry of Materials* **2017**, *29*, 3441–3453.

(10) Nowroozi, M. A.; Ivlev, S.; Rohrer, J.; Clemens, O. La_2CoO_4: a new intercalation based cathode material for fluoride ion batteries with improved cycling stability. *J. Mater. Chem. A* **2018**, *6*, 4658–4669.

(11) Schoonman, J.; Oversluizen, G.; Wapenaar, K. Solid electrolyte properties of LaF_3. *Solid State Ionics* **1980**, *1*, 211–221.

(12) Roos, A.; Aalders, A.; Schoonman, J.; Arts, A.; de Wijn, H. Electrical conduction and ^{19}F NMR of solid solutions $La_{1-x}Ba_xF_{3x}$. *Solid State Ionics* **1983**, *9-10*, 571–574.

(13) Breuer, S.; Gombotz, M.; Pregartner, V.; Hanzu, I.; Wilkening, M. Heterogeneous F anion transport, local dynamics and electrochemical stability of nanocrystalline $La_{1-x}Ba_xF_{3x}$. *Energy Storage Materials* **2019**, *16*, 481–490.

(14) Mohammad, I.; Witter, R.; Fichtner, M.; Anji Reddy, M. Room-Temperature, Rechargeable Solid-State Fluoride-Ion Batteries. *ACS Applied Energy Materials* **2018**, *1*, 4766–4775.

(15) Liu, L.; Yang, L.; Liu, M.; Li, X.; Shao, D.; Luo, K.; Wang, X.; Luo, Z. SnF_2-based fluoride ion electrolytes $MSnF_4$ (M = Ba, Pb) for the application of room-temperature solid-state fluoride ion batteries. *Journal of Alloys and Compounds* **2020**, *819*, 152983.

(16) Christe, K. O.; Wilson, W. W.; Wilson, R. D.; Bau, R.; Feng, J. A. Syntheses, properties, and structures of anhydrous tetramethylammonium fluoride and its 1:1 adduct with trans-3-amino-2-butenenitrile. *Journal of the American Chemical Society* **1990**, *112*, 7619–7625.

(17) Davis, V. K. et al. Room-temperature cycling of metal fluoride electrodes: Liquid electrolytes for high-energy fluoride ion cells. *Science* **2018**, *362*, 1144–1148.

(18) Bashian, N. H. et al. Electrochemical Oxidative Fluorination of an Oxide Perovskite. *Chemistry of Materials* **2021**, *33*, 5757–5768.

(19) Kurtz, W.; Roth, S. Neutron scattering and magnetization measurements in CsMnFeF$_6$. *Physica B+C* **1977**, *86-88*, 715–716.

(20) Momma, K.; Izumi, F. *VESTA*: a three-dimensional visualization system for electronic and structural analysis. *Journal of Applied Crystallography* **2008**, *41*, 653–658.

(21) Wilde, P.; Catlow, C. Defects and diffusion in pyrochlore structured oxides. *Solid State Ionics* **1998**, *112*, 173–183.

(22) Sayed, F. N.; Mandal, B. P.; Jain, D.; Pillai, C. G. N. S.; Tyagi, A. K. Improved ionic conductivity in NdGdZr$_2$O$_7$: Influence of Sc^{3+} substitution. *Journal of the European Ceramic Society* **2012**, *32*, 3221–3228.

(23) Subramanian, M.; Aravamudan, G.; Subba Rao, G. Oxide pyrochlores — A review. *Progress in Solid State Chemistry* **1983**, *15*, 55–143.

(24) van Dijk, M.; Burggraaf, A.; Cormack, A.; Catlow, C. Defect structures and migration mechanisms in oxide pyrochlores. *Solid State Ionics* **1985**, *17*, 159–167.

(25) Pannetier, J. Energie electrostatique des reseaux pyrochlore. *Journal of Physics and Chemistry of Solids* **1973**, *34*, 583–589.

(26) Picone, P.; Saegusa, N.; Srivastava, R.; Wong, C.; Morrish, A.; Wanklyn, B. Mössbauer study of the modified pyrochlores CsMFeF$_6$ (M = Mn, Ni). *Solid State Communications* **1982**, *44*, 279–283.

(27) Nowroozi, M. A.; Clemens, O. Insights on the Behavior of Conversion-Based Anode Materials for Fluoride Ion Batteries by Testing against an Intercalation-Based Reference Cathode. *ACS Applied Energy Materials* **2018**, *1*, 6626–6637.

(28) Nowroozi, M. A.; Wissel, K.; Donzelli, M.; Hosseinpourkahvaz, N.; Plana-Ruiz, S.; Kolb, U.; Schoch, R.; Bauer, M.; Malik, A. M.; Rohrer, J., et al. High cycle life all-solid-state fluoride ion battery with La$_2$NiO$_{4+d}$ high voltage cathode. *Communications Materials* **2020**, *1*, 1–16.

(29) Grenier, A.; Porras-Gutierrez, A. G.; Body, M.; Legein, C.; Chrétien, F.; Raymundo-Piñero, E.; Dollé, M.; Groult, H.; Dambournet, D. Solid Fluoride Electrolytes and Their Composite with Carbon: Issues and Challenges for Rechargeable Solid State Fluoride-Ion Batteries. *The Journal of Physical Chemistry C* **2017**, *121*, 24962–24970.

(30) Banks, E.; Deluca, J.; Berkooz, O. Preparation, magnetic properties and mossbauer study of the modified pyrochlores M^{II}M^{III}F$_6$A. *Journal of Solid State Chemistry* **1973**, *6*, 569–573.

(31) Menil, F. Systematic trends of the ^{57}Fe Mössbauer isomer shifts in (FeO$_n$) and (FeF$_n$) polyhedra. Evidence of a new correlation between the isomer shift and the inductive effect of the competing bond T-X ($\rightarrow$Fe) (where X is O or F and T any element with a formal positive charge). *Journal of Physics and Chemistry of Solids* **1985**, *46*, 763–789.

(32) Kurtz, W.; Geller, R.; Dachs, H.; Convert, P. Magnetic short range order in CsMnFeF$_6$. *Solid State Communications* **1976**, *18*, 1479–1483.

(33) Ati, M.; Sougrati, M.-T.; Rousse, G.; Recham, N.; Doublet, M.-L.; Jumas, J.-C.; Tarascon, J.-M. Single-Step Synthesis of FeSO$_4$F$_{1-y}$OH$_y$ (0 y 1) Positive Electrodes for Li-Based Batteries. *Chemistry of Materials* **2012**, *24*, 1472–1485.